
CONTROL SYSTEMS OF MOVING OBJECTS

Laboratory Study of Magnetic Properties of Hysteresis Rods for Attitude Control Systems of Minisatellites

D. S. Ivanov, M. Yu. Ovchinnikov, and V. I. Pen'kov

Keldysh Institute of Applied Mathematics, Russian Academy of Sciences, Miusskaya pl. 4, Moscow, 125047 Russia

e-mail: danilivanov@mail.ru

Received May 29, 2012

Abstract—Results of the experimental determination of the parameters of hysteresis rods made of soft magnetic materials used in passive attitude control systems to damp the perturbed motion of satellites relative to their center of mass are described. Based on the classical solution of the linear magnetization problem and an approximate solution of the problem of nonlinear magnetization in a variable magnetic field, it is shown that the considerable distortion in the experimental determination of the parameters is explained by eddy currents induced in the rods. To mitigate the effect of those currents, it is shown that the measurements must be performed when the frequency of the magnetic fields variation is not higher than 0.1–0.2 Hz. Using nonlinear magnetization theory, a procedure for the experimental determination of the parameters of hysteresis rods is developed. This procedure is augmented by the corresponding computer processing of weak valid signals. The procedure can be used for the choice of the parameters of damping devices included in satellite passive attitude control systems.

DOI: 10.1134/S1064230712060032

INTRODUCTION

Passive attitude control systems were widely used at the dawn of the age of cosmic research. Due to the emergence of small satellites at the end of the 20th century, especially due to the wide use of the so-called cubesats in recent years (satellites with a volume of 1 l and mass of 1 kg proposed by Prof. Twiggs from Stanford University in 1999), and to the involvement of universities and small innovation companies, the interest in passive attitude control systems has recently grown (see [1–3]). These are simple (at first glance) attitude control systems consisting, for example, of a strong permanent magnet and a set of hysteresis rods made of a soft magnetic material with low coercive force¹ that has high magnetic permeability in weak fields and is not saturated in the geomagnetic field. Such a system is called the passive magnetic attitude control system (PMACS). The permanent magnet aligned with the given satellite axis ensures its orientation along the magnetic induction vector of the local geomagnetic field. Hysteresis rods dissipate the energy of the perturbed angular motion of the satellite upon it is separated from the carrier rocket and ensure the asymptotic stability of the satellite's axis. Examples of satellites where PMACS was used are the USA's Transit-1B and Transit-2A, Injuns satellites, the German AZUR-1, European ESRO-1A and ESRO-1B, Japanese EXOS-A and EXOS-B, and the Czechoslovakian Magion satellites launched in the 1980s. A review of such satellites, the design of their attitude control systems, and dynamics issues were discussed in [4]. In the first decade of the 21st century, the Swedish Munin was launched (in 2000) [3], the USA's QuakeSat (in 2003) [5], the Japanese cubesat CUTE-/XI-IV (2003) [6], the USA's Spartnik, in which the PMACS is combined with the stabilization by the rotation about the satellite's axis along which the permanent magnet is oriented, and a liquid nutation damper (2003) [7], the Italian EduSAT (2011), the Russian TNS-0 No. 1 (2005), and the Dutch Delfi-C³ (2008) [8]. Several satellites with PMACS are under development, for example, the Russian nanosatellite TNS-0 No. 2, the cubesat BEESAT-3 of the Berlin University of Technology with an exotic hysteresis damping system in the form of a hysteresis plate [9], and the 3U-cubesat ConSat-1 of Toronto University (3U means that it consists of 3 interconnected cubesats). Great interest in the development and use of PMACSs has been expressed by universities and small companies entering the market of space services.

¹ Coercive force is a demagnetizing external magnetic field that must be applied to a magnetic material driven to saturation to reduce the magnetic induction inside the material to zero. The doubled coercive force is equal to the width of the principal hysteresis loop.

More rarely, hysteresis rods are used in passive gravitational and aerodynamic attitude control systems for small satellites. Among recent projects, one can mention the nanosatellite REFLECTOR with the mass of about 6 kg [10] with a gravity-gradient system launched in orbit in 2000 and MAK-A [11] with a passive aerodynamic attitude control system.

It is a common phenomenon when the time needed for a satellite to reach a steady-state mode and the attitude control accuracy in this mode differ considerably from the designed values. There are various causes of this phenomenon. For example, for a satellite with a PMACS, this may be the violation of conditions under which the satellite separates from the carrier rocket; the satellite can start rotating about the orientation axis, and this rotation is poorly damped by hysteresis rods [10]. Another cause may be the mismatch between the stated parameters of the rods and their actual values. The certified values of those parameters are determined by calculation, and they differ from the magnetic parameters of the sheet material and depend on the shape of the rods, and on the method used for their thermal treatment.

Doubts as to the magnitude of the coercive force are characteristic of designers of magnetic systems because it is well known that, in order to obtain low values of the coercive force, the magnetic material is annealed using an intricate timing chart. If the annealing is not used or if the annealing procedure even slightly deviates from the prescribed timing chart, the coercive force of the rod can be greater than that of the perfectly annealed rod by an order of magnitude; as a result, it is highly probable that the errors in the satellite attitude will be unacceptably high. Furthermore, the coercive force and other parameters of the annealed rods are very sensitive to mechanical deformations in the course of transportation and mounting. For these reasons, it is important to develop procedures for the routine control of their properties before the satellite assembly and to create an inexpensive laboratory facility for these purposes. In this study, we propose an approach to the experimental determination of the parameters of hysteresis rods, provide a theoretical justification of this approach, and discuss examples of measurements for the rods designed and manufactured for the use in satellite attitude control systems. This paper continues the study of control systems for mobile objects on facilities that are performed in the Keldysh Institute of Applied Mathematics, Russian Academy of Sciences [12–14].

To determine the rod parameters, a thorough analysis of the phenomena in the rods is needed [2, 4, 15]. To enable damping, rods are made of a magnetically soft material with a high relative magnetic permeability and low coercive force [1]. Typically, a magnetic hysteresis damper has the shape of elongated rod with a large length to diameter ratio. Its damping properties strongly depend on this ratio—the maximum efficiency is achieved for very elongated rods [2, 16]. In the case of small satellites, the rod length is limited by the satellite size and ensuring the desired length to diameter ratio (aspect ratio) results in reducing the total rod volume; therefore, the damper efficiency is reduced. Increasing the number of closely located rods does not improve the situation because the rods demagnetize each other, which is equivalent to reducing their aspect ratio. The rod size can be preliminary determined based on geometric considerations and basic design principles [2, 12, 14]. The most reliable method for determining the magnetic parameters of hysteresis rods is laboratory measurements.

There are several methods for measuring the magnetic characteristics of rods. For routine control, the induction method seems to be the most efficient one. The idea underlying this method is as follows. An elongated body is placed in a periodically changing solenoid field with known characteristics, and its magnetization is measured by the electromotive force induced in the measurement coil placed on the body according to the law of electromagnetic induction. It is known that an ellipsoidally shaped body with an arbitrary axes ratio is magnetized uniformly in a steady-state uniform field. A circular cylinder with a large ratio of the length to its diameter is magnetized almost uniformly. In the analysis of the measurement result, the nonuniformity of magnetization is typically neglected if the body shape is close to a strongly elongated cylinder.

The main integral characteristic of the damping magnetic hysteresis rod is the hysteresis loop. Using this loop, one can evaluate the loss of energy, that is, evaluate the damping properties of the rod and the residual magnetic moment determining the disturbing influence of the rod on the steady-state motion of the satellite. The residual magnetic moment strongly depends on the coercive force of the rod. If this force is less than the designed one, then the worse-case effect on the satellite in flight is that the time needed to reach the nominal (designed) motion (stabilization time) is longer than expected; that is, the transient process time increases. However, if the coercive force is much greater than the designed one (i.e., if the hysteresis loop is wide), the residual magnetization is high; as a result, large disturbing torques emerge that can cause the satellite to execute undesired angular motion. Therefore, when the satellite is assembled, it is necessary to be sure that the actual coercive force does not significantly differ from the designed force. If the actual coercive force differs from the designed force by a factor of two, there are no catastrophic consequences, even though such a value of the coercive force causes an error in the satellite attitude under the

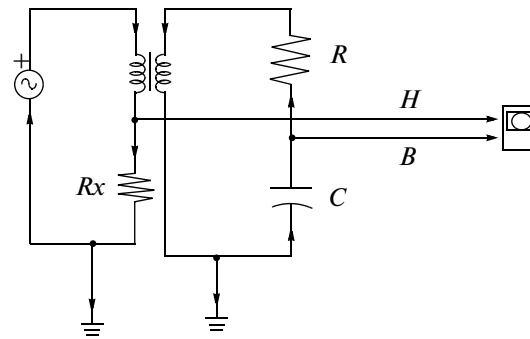


Fig. 1. Diagram of facility with an integration RC-circuit.

effect of the residual magnetization. Notice that, in the case of magnetically soft materials manufactured using the technology aimed at the maximum possible reduction in the coercive force, it is highly improbable that the actual coercive force is less than its certified value.

Let us track the history of the laboratory tests in the Keldysh Institute of Applied Mathematics to elucidate the sequence of steps that led to the development of the measurement procedure and to the improvement in the measuring characteristics of the laboratory equipment. The initially designed laboratory facility [17, 18] consisting of a transformer reducing the voltage of the standard electrical supply network down to 16 V, a variable resistor, a multilayer solenoid, a measuring coil, and an oscilloscope made it possible to evaluate the degree of nonuniformity of the rod magnetization in its length and the dependence of the induced electromotive force on the position of the rod relative to the Earth magnetic field. The use of the standard electrical supply network for feeding the solenoid taking into account the increased ohmic resistance of permalloys seemed to be quite natural because no special voltage generator for the primary coil was required.

The introduction of an integrating RC-circuit (integrator) (Fig. 1) and the simultaneous supply of voltage from the measuring resistor and the capacitor to the inputs of the GRS-60 oscilloscope enabled us to construct the hysteresis loop. In the first variant of the facility, the solenoid was 25 cm long, had the diameter 7.5 mm, and 2342 turns, while the measuring coil was 2 cm long, had the diameter 1.5 cm, and 1230 turns. The frequency of the magnetic field created by the solenoid was $f = 50$ Hz, which is equal to the frequency in the standard electrical supply network. For the verification purposes and for convenience, the numerical integration of the signal obtained from the measuring coil was used in addition to its analog integration.

Attempts to obtain reliable hysteresis loops in such a way ran into certain difficulties. It is seen from the typical curve (see Fig. 2) that, firstly, the disturbances are considerable even though they do not distort the shape of the hysteresis loop as a whole. Second, the maximum value of the induction turned out to be 0.35 T, which is about half of the certified value. Finally, the coercive force turned out to be about 25 A/m, which is more than by an order of magnitude greater than the certified value of 1.6 A/m for the rod made of permalloy 79NM 1 mm thick (GOST 10160-75: High-Precision Magnetically Soft Alloys).

While the insufficient magnitude of the magnetic induction can be explained, for example, by the insufficient magnitude of the magnetizing field and by the closure of a part of the magnetic flux within the measuring coil, the measured magnitude of the coercive force is unacceptable. In some cases, the magnetization curves were self-intersecting. One can find examples of self-intersecting hysteresis loops in the literature (see [19]). However, the emergence of such loops in the case under examination seemed to be at least strange. The detection of the causes of such a discrepancy between the expected results and the results of experiments performed on the laboratory facility [17, 18], perfection of this facility, the creation of a measurement procedure and the recommendations with respect to the investigation of hysteresis loops, and the results of application of this procedure are the aims of the present paper. Using inexpensive and widely available laboratory equipment, main characteristics of the magnetic hysteresis rods were determined. We are not aware of descriptions of similar laboratory equipment for the measurement and investigation of magnetic characteristics in the case of very weak output signal and low frequency of the remagnetizing field.

1. CONSTRUCTION OF THE HYSTERESIS LOOP USING ANALOG RC-CIRCUIT

To plot the hysteresis loop on the oscilloscope display using an integrating RC-circuit, an electric circuit shown in Fig. 1 is often used. The primary circuit is fed by the power supply. The current in the primary coil circuit can be controlled using a rheostat (not shown in Fig. 1). A measuring resistor R_x is sequentially included in the primary coil (solenoid) circuit. The voltage on this resistor is proportional to the current and, therefore, to the intensity of the magnetic field H . The influence of the current in the secondary circuit on H is neglected.

We denote by subscripts 1 and 2 the quantities related to the primary and secondary coils, respectively. The system of equations relating the voltage on the coils can be written as follows:

$$E + E_1 = R_1 I_1, \quad (1.1)$$

$$E_2 = R_2 I_2 + \frac{1}{C} \int I_2 dt. \quad (1.2)$$

Here, the induction electromotive force in the primary and secondary circuits is governed by the equations

$$E_1 = -N_1 \frac{d\Phi}{dt}, \quad E_2 = -N_2 \frac{d\Phi}{dt}; \quad (1.3)$$

the magnetic flux through the coils is

$$\Phi = BS + \mu_0 S_0 H; \quad (1.4)$$

and the intensity of the magnetic field inside the solenoid can be represented as

$$H = \frac{N_1 I_1}{l}. \quad (1.5)$$

Here, E is the power supply voltage, I_1 and I_2 are the currents, R_1 and R_2 are the total ohmic resistances of the circuits, C is the capacitance of the RC-circuit, N_1 and N_2 are the number of the coil turns, S and S_0 are the cross-section areas of the rod and the solenoid, respectively, B is the magnetic field induction inside the rod, μ_0 is the magnetic permeability of free space, and l is the solenoid length.

To construct the hysteresis loop, we choose R_2 and C sufficiently large. Then, the current in the secondary circuit and the voltage across the capacitor are small, and the last term in Eq. (1.2) may be neglected in the calculation of I_2 ; that is, $I_2 \approx E_2/R_2$. Now, Eq. (1.3) implies

$$I_2 \approx -\frac{N_2}{R_2} \frac{d\Phi}{dt}. \quad (1.6)$$

The voltage across the capacitor is determined by the chain of equalities

$$V_C = \frac{1}{C} \int I_2 dt = -\frac{N_2}{R_2 C} \Phi + V_0. \quad (1.7)$$

The voltage V_0 across the capacitor due to the initial charge can be assumed to be zero due to self-discharge and the discharge through the resistor R_2 and the coil. If we leave in Eq. (1.4) only the magnetic flux $B \cdot S$ in the rod (and neglect the magnetic flux in air because it is small compared with the flux in the rod), then we have

$$V_C \approx -\frac{N_2 S}{R_2 C} B. \quad (1.8)$$

Feeding the voltage from the measuring resistor R_x to the input X of the oscilloscope and the voltage V_C from the capacitor to the input Y , we approximately obtain the hysteresis loop $B = B(H)$ to a certain scale. Figure 2 depicts the hysteresis loop for the rod made of the 76NM alloy; the rod has a square section of $1 \times 1 \text{ mm}^2$, its length is 25 cm, and the integrator parameters are $R_2 = 400 \text{ K}\Omega$ and $C = 1 \text{ }\mu\text{F}$. The number of turns in the primary coil is $N_1 = 2342$, and its length is $l_1 = 25 \text{ cm}$, and the diameter is $D_1 = 7.5 \text{ mm}$. The number of turns in the secondary coil is $N_2 = 1550$, its length is $l_2 = 2 \text{ cm}$, and the diameter is $D_2 = 1.5 \text{ cm}$. The wire used to wind both coils is $d = 0.1 \text{ mm}$ in diameter. The frequency of the current source is $f = 50 \text{ Hz}$. The induction electromotive force $N_2 \frac{d\Phi}{dt}$ in the secondary circuit does not exceed

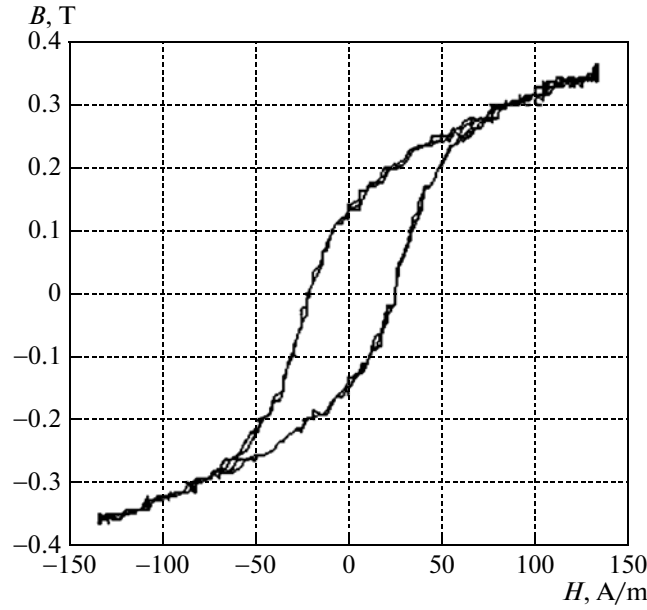


Fig. 2. Typical hysteresis curve at the frequency $f = 50$ Hz.

$N_2 2\pi f S B_S \approx 425$ mV, where B_S is the maximum magnitude of the magnetic field induction inside the rod. The current in the secondary circuit does not exceed 10^{-6} A, and the intensity of the magnetic field H induced by this coil's current does not exceed 0.01 A/m, which is negligibly small compared with the values of H in the plot. Exactly this assumption was made in the beginning of the present section. Using relation (1.8), we obtain an estimate of the voltage across the capacitor $V_C \leq 3$ mV, which is also small compared with $I_2 R_2 \approx 400$ mV. Thus, the main assumptions used in the construction of the hysteresis loops are fulfilled for the facility under examination.

Using the proposed laboratory facility, we obtained hysteresis loops with the coercive force exceeding the certified value by an order of magnitude, and the maximum induction was insufficient for the material used. The loop could have self-intersections, which contradicts the physical nature of the process (Fig. 2). To reveal the cause of the significant discrepancy between the experimental and the expected curves, we evaluate the influence of the phase distortions in the integrator. The evaluation is performed under the assumption that $B = \mu_{\text{rod}} \mu_0 H$, the magnetic permeability of the rod is $\mu_{\text{rod}} = \text{const}$, and

$$H = H_0 \sin \omega t, \quad (1.9)$$

where ω is the remagnetization angular velocity. In this case, the hysteresis loop is obviously a straight line segment.

By changing to complex form, it can be easily shown that the signal V_C taken from the capacitor and interpreted as the magnetic induction B in the rod is shifted in phase by the quantity

$$\alpha = \arctan \frac{1}{\omega R_2 C} \quad (1.10)$$

so that

$$B = \mu_{\text{rod}} \mu_0 H_0 \sin(\omega t - \alpha). \quad (1.11)$$

Equations (1.9)–(1.11) define an ellipse in the plane (H, B) rather than a line segment. The points of intersection of this ellipse with the horizontal axis determine the error introduced into the value of the coercive force H_C :

$$\Delta H_C = H_0 \sin \alpha \approx \frac{H_0}{\omega R_2 C}. \quad (1.12)$$

Approximately, we may set

$$H_0 \approx \frac{B_S}{\mu_{\text{rod}} \mu_0}.$$

Then,

$$\Delta H_C \approx \frac{B_S}{\omega R_2 C \mu_{\text{rod}} \mu_0}. \quad (1.13)$$

In the case under examination, $\omega R_2 C \approx 125$, $\mu_{\text{rod}} \approx 9000$, $B_S \approx 0.7 \text{ T}$, the phase shift $\alpha = \frac{1}{125} \text{ rad}$ ($\approx 0.46^\circ$) is small, and the error $\Delta H_C \approx 0.5 \text{ A/m}$ emerging due to the phase shift, which is about a third of the certified value, does not explain the discrepancy between the experimental and expected hysteresis loops either (see [20]).

If we require that the error ΔH_C does not exceed, for example 10% of H_C , then we obtain the inequality that is useful for choosing the parameters of the integrator:

$$\omega R_2 C \geq \frac{B_S}{0.1 \mu_{\text{rod}} \mu_0 H_C}. \quad (1.14)$$

It is worth noting that the quantity $\omega R_2 C$ also shows the factor by which the integrator attenuates the input signal fed at its input. In the case under consideration, we must have $\omega R_2 C \geq 390$ in order to ensure that the error does not exceed 10%. However, the useful signal in this case decreases by a factor of three compared with that represented in Fig. 2, and the error level becomes significant.

The above analysis and the mathematical modeling of the integrating RLC circuit enable us to draw the following conclusions: (1) the properties of the integrator are not the cause of the significant difference between the experimental and the expected curves; (2) the accuracy of the analog integration is close to its limit because the estimates above indicate an unacceptably low level of the useful signal when the requirement for the acceptable measurement error is fulfilled. An acceptable explanation of the considerable difference between the experimental and expected results can be obtained using the theory of linear magnetization of an infinite circular cylinder in a variable magnetic field.

2. LINEAR MAGNETIZATION OF AN INFINITE CIRCULAR CYLINDER: ANALYTIC SOLUTION

Consider an infinitely long circular cylinder of radius a with the magnetic permeability μ wound by a wire with an electric current, which induces the field $H_0 \cos \omega t$. The solution of the Maxwell equations

$$\text{curl } \mathbf{E} = -\frac{\partial \mathbf{B}}{\partial t}, \quad (2.1)$$

$$\text{curl } \mathbf{H} = \mathbf{j} \quad (2.2)$$

for the linear dependence $\mathbf{B} = \mu \mu_0 \mathbf{H}$, $\mathbf{j} = \rho \mathbf{E}$ subject to the boundary condition $H(a) = H_0 \cos \omega t$ is reduced to the solution of the modified zero-order Bessel equation

$$\frac{\partial^2 B_z}{\partial v^2} + \frac{1}{v} \frac{\partial B_z}{\partial v} - B_z = 0, \quad (2.3)$$

where $v = r\sqrt{ip}$, B_z is the field along the cylinder axis in the steady-state mode, $B_0 = \mu \mu_0 H_0$, $p = \mu \mu_0 \omega / \rho$, ρ is the specific resistance of the rod, r is the distance from the rod axis, and i is the imaginary unit. Notice that $r = 0$ is a singular point of Eq. (2.3). It was shown in [21] that, in the steady-state mode, the field \tilde{B}_z in the cylinder is given in complex form in terms of the Bessel function of the first kind I_0 by the expression

$$\tilde{B}_z = \frac{I_0(ip^{1/2}r)}{I_0(ip^{1/2}a)} B_0 e^{i\omega t}. \quad (2.4)$$

In the same book, the following expressions were obtained by separating the real part:

$$B_z = \left\{ \frac{\text{ber}_0^2(p^{1/2}r) + \text{bei}_0^2(p^{1/2}r)}{\text{ber}_0^2(p^{1/2}a) + \text{bei}_0^2(p^{1/2}a)} \right\}^{1/2} B_0 \cos(\omega t + \alpha), \quad (2.5)$$

Table 1. Calculation results for the coercive force and the error in its determination for various frequencies of the remagnetizing field

Example (figure)	Field frequency, Hz	Coercive force H_C , A/m	Error in the determination of the coercive force ΔH_C , A/m
1 (fig. 3)	50	20	20
2 (fig. 4)	1	0.4	0.4
3 (fig. 5)	0.2	0.08	0.08

$$\alpha = \arg \frac{I_0((ip)^{1/2}r)}{I_0((ip)^{1/2}a)}. \quad (2.6)$$

Here, ber and bei are Kelvin's functions.

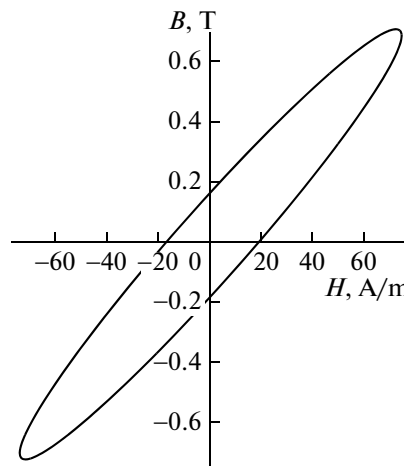
Let us discuss the computational results based on formulas (2.4)–(2.6) for the rod in the shape of a circular cylinder of the diameter 1.128 mm ($a = 0.564$ mm) and length 25 cm. The cross-section area of this cylinder is 1 mm², which equals the cross-section area of the actual rod (i.e., 1 mm²). Furthermore, we assume that the number of turns of the solenoid is $N_1 = 2342$, the current is $i_0 = 8$ mA, B is the integral average over the rod cross-section, H is the solenoid field, $\mu_{\text{rod}} = 8000$, and $\rho = 5 \times 10^{-7} \Omega \cdot \text{m}$ (79NM alloy). The results are presented in Table 1. In Example 1, we have the loop width $H_C \approx 20$ A/m rather than $H_C = 0$, which exceeds the expected actual value $H_C = 1.6$ A/m more than by an order of magnitude. It is clear that if there is no phase shift in the cross-section, we should have $\Delta H_C = 0$ for any non-uniformity of the magnetization. Therefore, the main cause of the error ΔH_C is the phase shift due to eddy currents in the rod. A natural way to reduce the nonuniformity of magnetization and the phase shift is to reduce the frequency f of the power supply.

In Example 2, the result is closer to the expected one, but it is still unacceptable.

In Example 3, the magnetization is almost uniform over the rod cross-section. The error is $\Delta H_C \approx 0.08$ A/m, which is 5% of the certified value; this is acceptable for routine control.

It is useful to describe a simple method for determining H_C for the case of linear magnetization that does not require the construction of the curves depicted in Figs. 3–5. Changing in (2.4) to the dimensionless quantities $p_0 = a\sqrt{p}$ and $x = r/a$, it is easy to see [10] that H_C/H_0 depends only on p_0 . This dependence is illustrated in Fig. 6. For $p_0 \leq 0.5$, this dependence can be described by the formula

$$H_C/H_0 = 0.1248p_0^2 \quad (2.7)$$

**Fig. 3.** Function $B = B(H)$ for the frequency $f = 50$ Hz.

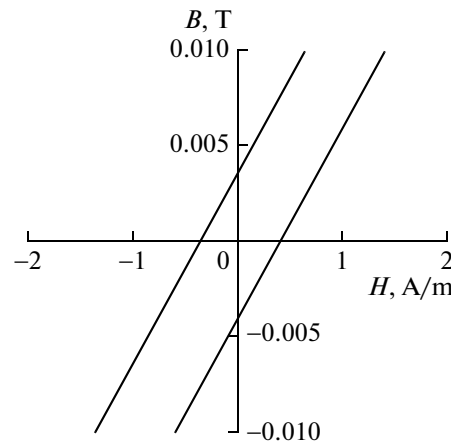


Fig. 4. A fragment of the function $B = B(H)$ for the frequency $f = 0.1$ Hz.

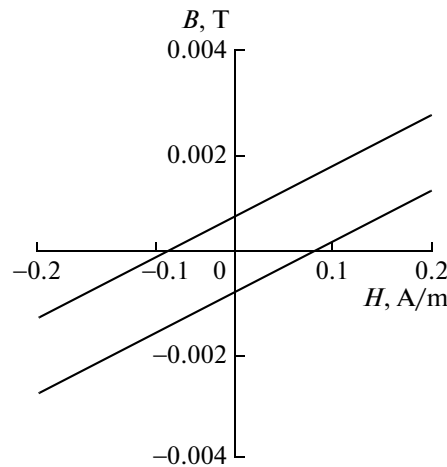


Fig. 5. A fragment of the function $B = B(H)$ for the frequency $f = 0.2$ Hz.

with an error not greater than 0.2%. This formula should be used for small p_0 . The approximate values of p_0 for the corresponding magnetization frequencies and for the rectangular rod with the cross-section $1 \times 1 \text{ mm}^2$ are given in Table 2.

The condition of magnetization linearity imposes a constraint on H_0 . Approximately, we may set

$$H_0 \approx \frac{B_s}{\mu_{\text{rod}} \mu_0}. \quad (2.8)$$

The curves in Figs. 3–5 are obtained with regard to this relation for $B_s = 0.75 \text{ T}$; since the real-life rods have a finite length, one must use the magnetic permeability of the rod μ_{rod} as the magnetic permeability of the material μ for the calculation of p_0 .

In the practical application of the linear magnetization model described above, one can only expect to obtain estimated values of the coercive force and the magnetic permeability due to considerable uncer-

Table 2. Dependence of p_0 on frequency

$f, \text{ Hz}$	0.1	0.2	0.5	1	5	50
p_0	0.063	0.09	0.14	0.2	0.45	1.4

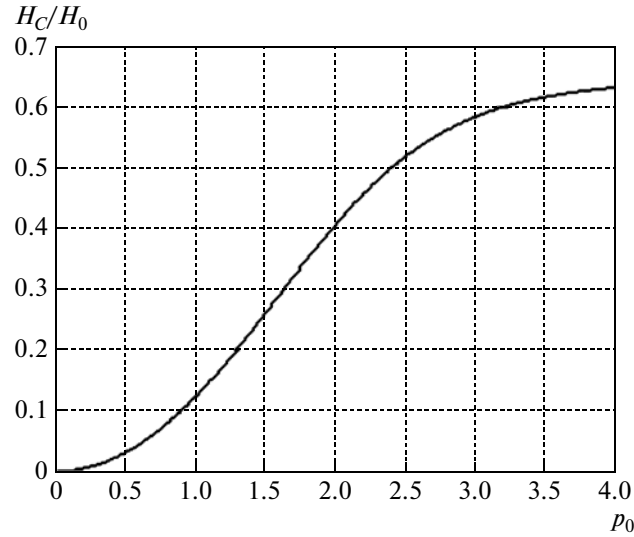


Fig. 6. H_C/H_0 as a function of p_0 .

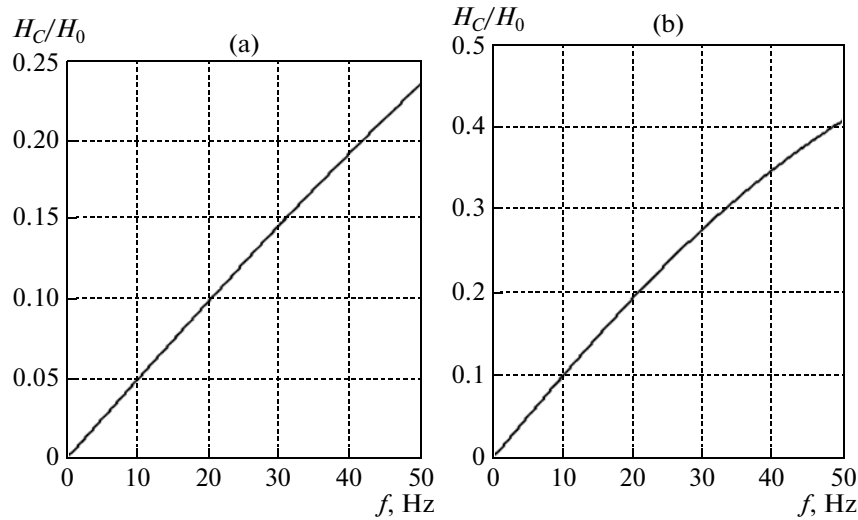


Fig. 7. The function H_C/H_0 for the cross-sections 1×1 (a) and 1×2 mm² (b).

tainty in the choice of H_0 and μ_{rod} . In [12, 13], a formula for the demagnetization coefficient of the cylindrical rod was presented:

$$N = (\ln(1.2p) - 1)/p,$$

where $p = L/d$ is the rod aspect ratio. For a rod with the cross-section 1×1 mm² (the experimental results for which are illustrated in Fig. 2), the demagnetization coefficient found by this formula can take the values from 7.5×10^{-5} to 1.4×10^{-4} depending on the method used to calculate the aspect ratio. Respectively, the rod magnetic permeability can take the values from $\mu_{\text{rod}}^{\min} = 5600$ to $\mu_{\text{rod}}^{\max} = 12400$, and the ratio H_C/H_0 can take the values from 0.23 to 0.34. For $B_S = 0.75$ T, we have $H_C \approx 19$ A/m, which is close to the initial experimental value $H_C \approx 25$ A/m.

Figures 6 and 7 (obtained using (2.7)) show H_C/H_0 as a function of frequency for the square rod 1×1 mm² and the rectangular rod 1×2 mm² for $\mu_{\text{rod}}^{\min} = 8000$. The majority of experiments were performed with these rods.

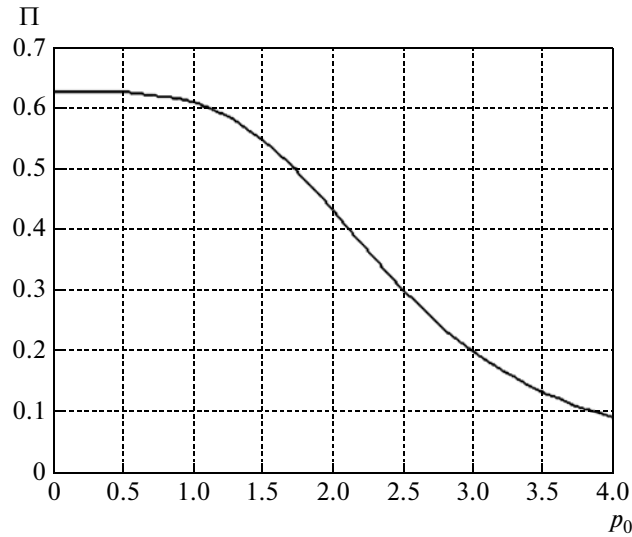


Fig. 8. The function $\Pi(p_0)$.

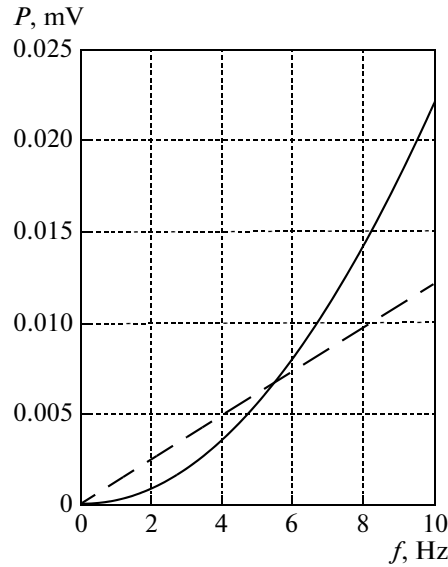


Fig. 9. Powers of the ohmic and hysteresis losses depending on frequency for a rod.

For small frequencies f , one can use the approximate expressions $H_C/H_0 = 0.005f$ for $S = 1 \text{ mm}^2$ and $H_C/H_0 = 0.01f$ for $S = 2 \text{ mm}^2$. The following expression for the average power of the ohmic losses in the rod under linear remagnetization is useful (see [10]):

$$P_{med} = \frac{VB_0^2\omega^2a^2}{\rho}\Pi(p_0). \quad (2.9)$$

The function $\Pi(p_0)$ is illustrated in Fig. 8. For small $p_0 < 0.5$ and, correspondingly, low frequencies (see Table 2), we have

$$P_{med} \approx \frac{2.5VB_0^2a^2f^2}{\rho}. \quad (2.10)$$

Figure 9 illustrates the average power of ohmic (solid line) and hysteresis (dashed line) losses depending on the frequency for the rod with the cross-section $S = 1 \text{ mm}^2$, length 25 cm, $\mu_{rod} = 8000$, $B_0 = 0.75 \text{ T}$,

and $\rho = 5 \times 10^{-7} \Omega \cdot \text{m}$. The hysteresis losses were calculated by the formula $P_{\text{hyst}} = 4H_C B_S V f$ for $H_C = 1.6 \text{ A/m}$, $B_S = 0.75 \text{ T}$, and $V = Sl = 0.25 \times 10^{-6} \text{ m}^3$. For the frequencies lower than 5 Hz, the hysteresis losses are greater; for the frequencies higher than 5 Hz, the ohmic losses are greater. Taking into account the ohmic losses, we can more accurately evaluate the dissipation of the satellite angular motion energy upon separation from the carrier when the angular velocity is high.

The validity of results obtained using the linear model depends on the degree of the rod magnetization. The results in which the maximal induction in the greater part of the rod cross-section does not exceed B_S are fairly realistic. The plot in Fig. 9 was obtained under the condition that the induction has its maximum B_{max} on the lateral surface of the rod and $B_{\text{max}} = B_S = 0.75 \text{ T}$, the rod cross-section area is $S = 1 \text{ mm}^2$, its length is 25 cm, $\mu_{\text{rod}} = 8000$, and $\rho = 5 \times 10^{-7} \Omega \cdot \text{m}$.

3. NONLINEAR MAGNETIZATION OF A ROD BY THE LAW $B = B_S \tanh(\sigma H)$: NUMERICAL SIMULATION

It was mentioned in the end of Section 1 that the modification of the facility illustrated in Fig. 1 by replacing the analog integration using an RC-circuit with numerical integration could improve the useful signal at the entry of the oscilloscope by two orders of magnitude. However, the difficulties due to the low useful signal still exist because when the frequency of the power supply decreases from 50 to 0.1–0.2 Hz the voltage fed at the input of the oscilloscope is correspondingly decreased. To refine the range of acceptable frequencies, more accurately describe the distortions of the hysteresis loop shape and the ohmic losses by eddy currents, a more accurate mathematical model was developed. In this model, the nonlinear magnetization curve $B = B_S \tanh(\sigma H)$ was used. The hyperbolic tangent with the parameter σ was chosen because the shape of the magnetization curve $B = B_S \tanh(\sigma H)$ is close to the shape of the hysteresis loop. The parameters σ and B_S are fitted when the hysteresis loop is approximated by the tangent-like curve.

The magnetic permeability is assumed to be nonconstant over the rod cross-section; it is specified as a function of r . The primary coil circuit is fed by a voltage source providing a prescribed voltage or by a current source providing a prescribed current. Recall that the source of electromotive force is defined as a source that provides the voltage independent of the load. An example of such a source is the standard power supply network in which the voltage is almost invariably 220 V. The current source provides a prescribed current independently of the resistance of the external circuit and on the voltage on its terminals. In practice, a current source is a source of electromotive force whose internal resistance is much greater than the resistance of the external circuit and the load.

As a starting point for constructing the improved mathematical model, we use the model used in [21]; that is, we consider an infinitely long circular cylinder in the uniform solenoidal field. If the function $B = B(H)$ is nonlinear, the method of separation of variables used to obtain analytic solution (2.4) is inapplicable. To find a numerical solution, the cylinder cross-section was subdivided into layers by concentric circles r_k , $k = 1, \dots, n$. Both uniform and nonuniform grids condensing in the vicinity of $r_1 = 0$ were used because this point is a singular point of the equations. To resolve the indeterminacy at the point $r_1 = 0$, linear interpolation was used. The transition from partial differential equations to the system of ordinary differential equations is described in the Appendix and in [10] in more detail. Note that the resultant systems of equations are stiff, and they must be solved using appropriate numerical methods.

For $n = 50$, the analytic and numerical solutions to Eqs. (2.1), (2.2) are fairly close to each other. In some numerical experiments, the dependence of the current in the solenoid on time was determined based on the actual data obtained using a digital oscilloscope. The actual discrete function was approximated by a truncated Fourier series. In addition to the perfect source of electromotive force with a zero internal resistance, sources with nonlinear internal resistance were used; the voltage drop on these sources was specified in the form $E = aI + bI^3$ or $E = E_S \tanh(aI)$.

In the numerical simulation, dissipation of the magnetic flux was simulated. Using weighting coefficients, the magnetic fluxes in the rod layers in which the magnetic force lines can close inside the solenoid or the measuring coil were cut off partially or completely. The indexes of these layers were specified based on general considerations: the force lines emanating from the central layers do not close, while the lines emanating from the peripheral layers can close inside the coils.

Intensive computations with various weighting coefficients, magnetic permeabilities of layers, and nonlinearities in the resistances of power supply sources (within reasonable limits) did not clearly reveal the self-intersection phenomenon. Several self-intersection situations were observed when the integration

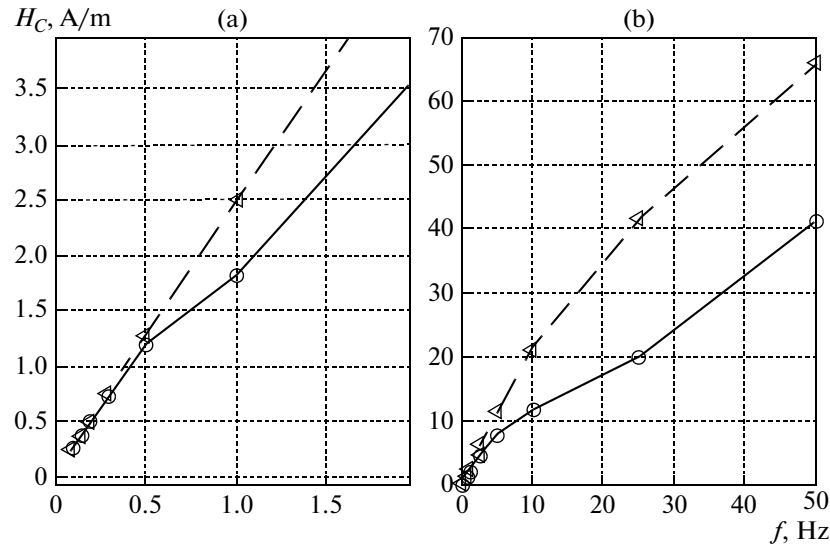


Fig. 10. Coercive force H_C as a function of frequency.

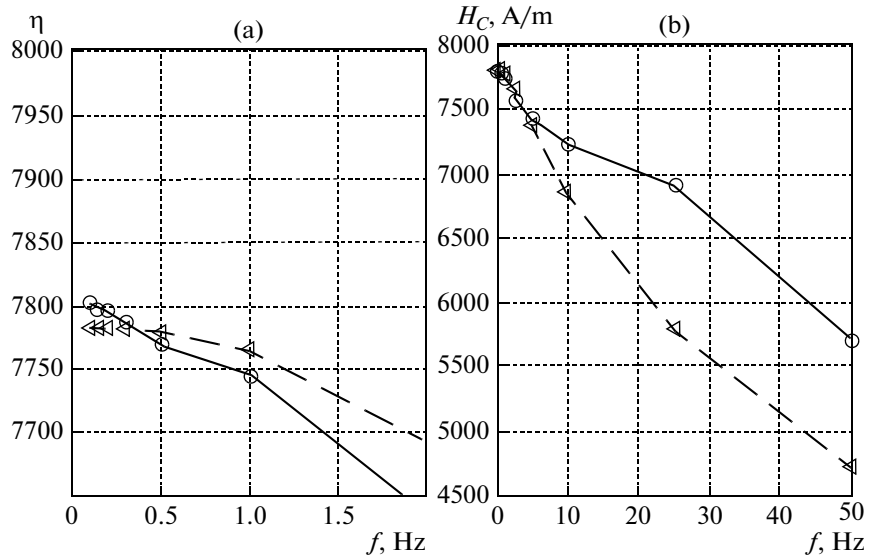


Fig. 11. Magnetic permeability μ_{rod} as a function of frequency.

was insufficiently accurate (this can be interpreted as simulation of disturbances) and, sometimes, when artificial additional constant phase shift between the oscilloscope channels was introduced.

Let discuss the dependences of the coercive force H_C (Fig. 10) and the magnetic permeability μ_{rod} (Fig. 11), which is calculated based on the linear segment of the loop plot, on frequency. These dependences were obtained by the numerical integration of the nonlinear model. They were calculated for the rod with the cross-section $1 \times 2 \text{ mm}^2$, length 25 cm, and the magnetic permeability $\mu_{rod} = 8000$. The symbol \circ marks the curves obtained when the solenoid was fed by an EMF source, and the symbol \triangleright marks the curves obtained when it was a current source. In both cases, the maximum magnetization was close to saturation. For the frequency of 0.2 Hz, we have $\Delta H_C = 0.5 \text{ A/m}$. Recall that this quantity is the error due to the emergence of eddy currents at this frequency. Based on the linear analysis, this error was estimated to be about 0.15 A/m. The magnetic permeability is less distorted. At the frequency of 0.2 Hz, its difference from the “true” value (8000) is about 3%.

The difference in the curves in the cases when the solenoid is fed from an EMF source or from a current source and both of them ensure the magnetization almost to saturation is explained by the nonlinearity of

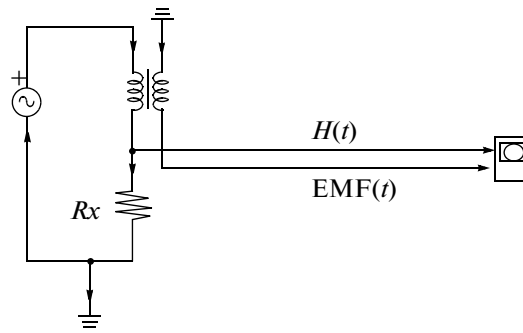


Fig. 12. Diagram of the measuring facility.



Fig. 13. Facility for the investigation of hysteresis rod properties.

the problem, which implies the difference in the spectra of the solenoid magnetic field intensity. This fact is confirmed by numerical results. Note that the mathematical model with a current source better suits the first facility variant with a step-down transformer and relatively high total resistance in the solenoid circuit. When the facility is fed from the G6-46 generator (the second facility variant, Figs. 12, 13), the model with an EMF source is more adequate. In the latter case, both the solenoid and the measuring coil had an increased number of turns ($N_1 = 18000$ and $N_2 = 30000$). The computation time needed for integration on an ordinary desktop were as high as several hours for low frequencies and the model with the EMF force; in the case of the current source, the time was by an order of magnitude shorter. For the frequencies lower than 0.5 Hz, the results obtained using these models are practically identical. The dependences of the ohmic and hysteresis losses on frequency are close to those found earlier (see Fig. 9).

Thus, using the numerical simulation of the remagnetization process and a nonlinear magnetization law, the range of acceptable frequencies is refined, and the distortions of the hysteresis loop shape and ohmic losses due to eddy currents are determined more accurately.

4. NUMERICAL SIGNAL INTEGRATION: EXPERIMENTAL RESULTS

The low magnitude of the useful signal and its additional attenuation by a factor of ωRC (see (1.4)) by the integrator force us to reject analog integration and replace it by numerical integration using a digital oscilloscope. The basic diagram of the facility is shown in Fig. 12. The facility itself is depicted in Fig. 13.

In this facility, the whole signal $E_2 = -N_2 \frac{d\Phi}{dt}$ rather than the signal attenuated by a factor of ωRC is fed to the input of the second oscilloscope channel. The measurement results are stored in digital form in the oscilloscope memory, and then are passed through a USB port to a computer for processing. The values obtained by digitizing the analog signal obtained from the oscilloscope are converted to volts and related

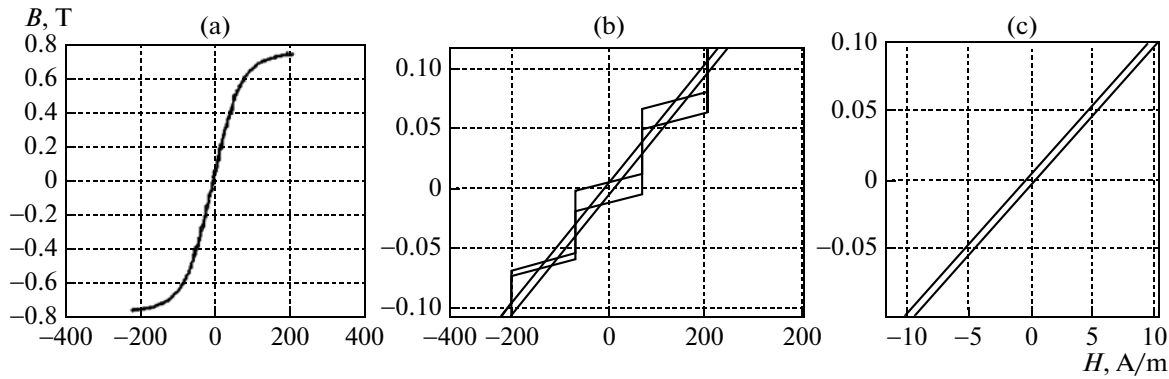


Fig. 14. The function $B = B(H)$.

to time using known calibration coefficients. The processing mainly aims at the thorough centering of the data in the second channel (i.e., determining zeros) and the corresponding shift. The preliminary data centering is performed by a computer program automatically using one of the two methods—range based or integrally based. In the first method, zero is set at the arithmetic mean of the minimum and maximum values; in the second method, it is the integral mean value. The further centering of the input data is performed interactively based on a visual judgment about the periodicity of the integration result and the closeness of the hysteresis loop. The integration of the data in the second channel (i.e., E_2), gives the magnetic flux Φ ; then, it is centered, and the mean over the cross-section Φ/S is taken as the induction B in the rod. Upon fitting, the hysteresis curves take their final shape. Before processing the actual measurements, it is useful to perform a mathematical modeling of this procedure.

4.1. Simulation of the Measurement Processing Procedure

To simulate the measurement processing procedure, we use the data obtained using the numerical simulation described in Section 3. These data were used as the reference ones, and the results of subsequent transformations were compared with them. The transformations involved superimposing noise and digitizing the reference data and transforming then from volts and seconds to the display coordinates taking into account the fact that the oscilloscope display has 1000 markings numbered from 0 to 999 on the horizontal axis and 256 markings (steps) numbered from 0 to 255 on the vertical axis. Then, these pseudoreal data were processed as the actual data. Simulation enabled us to evaluate the effect of digitization, noise, fitting parameters, and other factors on the reliability of results and estimate the limits of the proposed method.

Figure 14a shows the curve $B = B(H)$ plotted after the unfitted data processing and the reference curve. It is seen that these curves are globally almost identical, but there are considerable local differences (Fig. 14b). For example, it is difficult to conclude based on Fig. 14c that the width of the original loop is $H_C \approx 0.5$ A/m. Figure 14c shows fragments of the original curve $B = B(H)$ and the smoothed curve. These curves are almost identical.

The noise has a negative effect at deep saturation, which results in the emergence of long horizontal fragments in the EMF plot. On these segments, the useful signal that is close to zero is “covered” by noise, which increases the integration error. To attenuate the influence of noise in real-life experiments, the measuring coil was shunted by a capacitor. Its capacitance (≈ 100 μF) was chosen so that the global variations in the curves on the display were not discernable.

4.2. Measurement Processing

No special measures (such as screening or thermostating) were used in the experiments. Some time was reserved to warm up the equipment and to wait until the output of the signal generator is in the steady-state mode. Some experiments were discarded upon visual verification of the results.

Consider the results of processing one of three identical experiments at the frequency $f = 0.2$ Hz for the rods 25 cm long with the cross-section area $S = 1 \times 2$ mm² for $|H_e| \leq 350$ A/m.

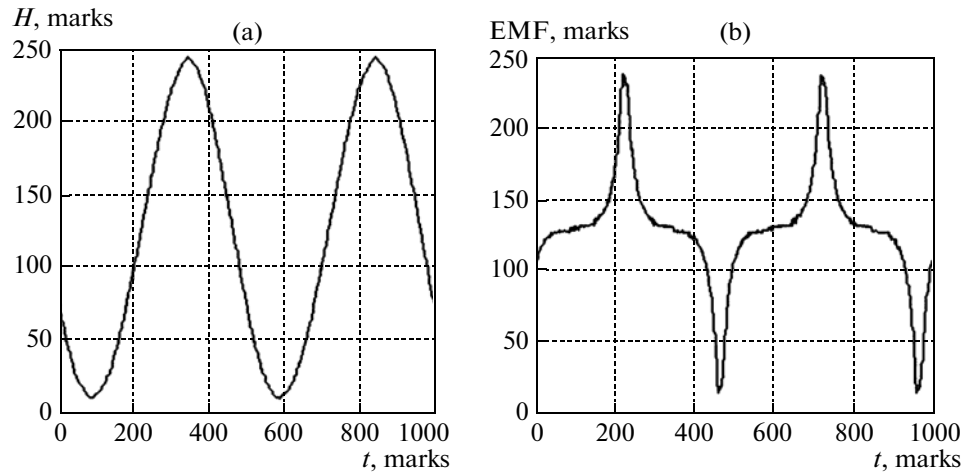


Fig. 15. Experimental data received by the computer from two oscilloscope channels.

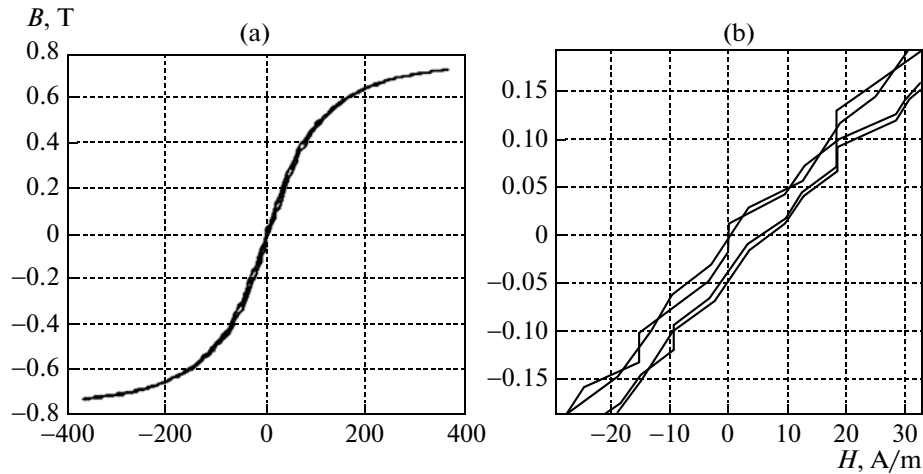


Fig. 16. The function $B = B(H)$ based on the experimental data.

Figures 15a and 15b illustrate the experimental data obtained by the computer from two oscilloscope channels. The first channel gets the voltage on the measuring resistor R_x in the solenoid circuit; the second channel gets the voltage on the terminals of the measuring coil. The voltage on the resistor determines the current and, therefore, the intensity H_e of the solenoid magnetic field. The voltage tapped off the coil is proportional to the derivative $\frac{d\Phi}{dt}$ of the magnetic flux with respect to time; upon integration, it determines the average induction B over the cross-section. We neglect the voltage drop due to the coil resistance because the current is low. Figures 17a and 17b show the unsmoothed curve $B = B(H)$, and Figs. 17a and 17b show the corresponding smoothed curve. Using the linear part (Fig. 17a), it is easy to determine the magnetic permeability of the rod $\mu_{\text{rod}} \approx 4900$; in the vicinity of zero (Fig. 17b), we have $H_C \approx 2.9$ A/m.

In the two other experiments, two values for the magnetic permeability μ_{rod} : ≈ 4800 and 4900 and two values for the coercive force $H_C \approx 2.8$ A/m and ≈ 3.1 A/m were obtained. These data are provided to demonstrate the stability of results. If the length of the low-slope parts in the vicinity of saturation decreases, the distortion due to noise decreases; therefore, it is reasonable to use moderate rod magnetization. Deep saturation used to refine the limiting loop as much as possible can give an opposite result. Processing the result of the experiment with a lower magnitude of the solenoid field $|H_e| \leq 150$ A/m, we obtain $\mu_{\text{rod}} \approx 5100$ and $H_C \approx 2.6$ A/m.

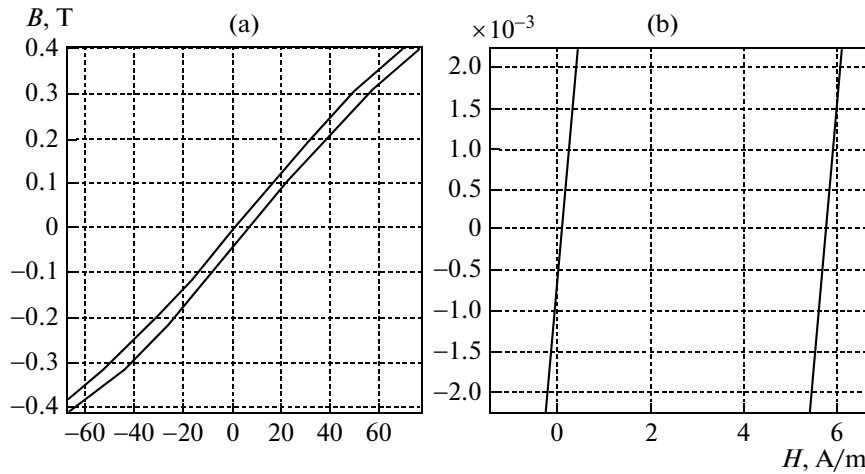


Fig. 17. Fragments of the function $B = B(H)$ based on smoothed data.

Taking into account the experimental results, we conclude that, in the range of the external magnetic field ± 60 A/m, the magnetic permeability of the rod is $\mu_{\text{rod}} \approx 5000$ and $H_C \approx 2.9 \pm 0.5$ A/m. Here, ± 0.5 A/m is the theoretical estimate of the error (Fig. 10) introduced by the Foucault currents at the frequency $f = 0.2$ Hz. The maximal magnetic permeability is somewhat greater— $\mu_{\text{rod}}^{\text{max}} \approx 5300$. The saturation induction (e.g., see Fig. 16a) is close to the certified value $B_S = 0.75$ T. For a rod 10 cm long with the cross-section area $S = 1 \times 1 \text{ mm}^2$, we obtained $\mu_{\text{rod}} \approx 2400$ and $H_C \approx 4.1$ A/m.

Let us estimate the influence of the error in determining the coercive force, for example, on the accuracy of the satellite orientation in the steady-state mode when PMACS is used. For definiteness, we use the parameters of the attitude control system of the Munin nanosatellite [2]. This satellite was equipped with six rods of the length 15.5 cm and the cross-section area $1 \times 1 \text{ mm}^2$ and with a permanent magnet with the dipole moment 0.3 Am^2 aligned with the longitudinal axis of the satellite. Computations show that an error by a factor of two in the determination of the coercive force increases the deviation of the satellite's longitudinal axis from the induction vector of the local geomagnetic field only by 1.5° . The main contribution to the orientation error is made by two other factors—forced oscillations of the satellite's axis along which it must be oriented (for Munin, the amplitude of these oscillations is about 10°) and the residual rotational velocity about the longitudinal axis, which is weakly damped by hysteresis rods. The second cause was determining for another nanosatellite with a PMACS—TNS-0 No. 1—in which the deviation of the longitudinal axis from the desired direction was as high as 45° [22].

CONCLUSIONS

The main result of this paper is a simple procedure for the evaluation of the magnetic characteristics of hysteresis rods used in satellite passive attitude control systems to dissipate the energy of disturbed angular motion. The basic characteristics determining dissipation are the coercive force and the magnetic permeability of the rod. The proposed procedure makes it possible to measure the magnetic permeability accurate to 10%. The error in determining the coercive force can be as high as 100%; however, taking into account the fact that the coercive force is small for magnetically soft materials such as permalloy 79NM, such an error is acceptable from the viewpoint of its influence on the steady-state motion.

Using the classical solution of the Maxwell equations, magnetization of a long cylinder in a variable magnetic field was analyzed and methods for evaluating the losses due to eddy currents and for determining the coercive force were developed. Using a typical rod as an example, it was shown that hysteresis losses are dominant for the frequencies lower than 5 Hz, while ohmic losses are dominant for the frequencies higher than 5 Hz. The magnitude of the coercive force determining the distortion of the hysteresis loop by eddy currents restricts the feasible remagnetization frequencies that can be used in experiments.

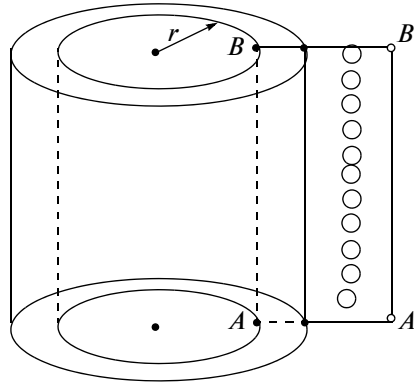


Fig. 18. Schematic view of a rod.

APPENDIX

TRANSITION FROM PARTIAL DIFFERENTIAL EQUATIONS TO A SYSTEM OF ORDINARY DIFFERENTIAL EQUATIONS

We write Maxwell system of equations (2.1)–(2.2) in integral form

$$\oint_{K_1} \mathbf{E}(t) d\mathbf{l} = -\frac{\partial \Phi}{\partial t}, \quad (\text{A.1})$$

$$\oint_{K_2} \mathbf{H}(t) d\mathbf{l} = I, \quad (\text{A.2})$$

where Φ is the magnetic flux, I are the macroscopic conduction currents,

$$\Phi = \iint_{S_1} \mathbf{B} d\mathbf{S}, \quad (\text{A.3})$$

$$\mathbf{I} = \iint_{S_2} \mathbf{j} d\mathbf{S}, \quad (\text{A.4})$$

$$\mathbf{j} = \frac{1}{\rho} \mathbf{E}, \quad (\text{A.5})$$

K_1 and K_2 are closed contours, and S_1 , S_2 are the areas of these contours. We solve this system in cylindrical coordinates, while neglecting the nonuniformity along the cylinder length. Due to symmetry, the unknown quantities E and H appearing in the equations depend only on the coordinate r and on time t .

As the contour K_1 , we take the circle of radius r centered at the point $r_1 = 0$; the contour K_2 is formed by the straight segment inside the rod that is at the distance r from its longitudinal axis and the line $BB'A'A$ that closes the contour outside the rod (Fig. 18). Then, Eqs. (A.1) and (A.2) can be written as

$$E(r, t) = -\frac{1}{r} \frac{\partial}{\partial t} \int_0^r B(r, t) r dr, \quad (\text{A.6})$$

$$H(r, t) + \frac{1}{l} \int_{BB'A'A} \bar{H}_e \cdot d\bar{l} = \frac{N_1 \cdot I_1}{l} + \frac{1}{\rho} \int_r^a E(r, t) dr, \quad (\text{A.7})$$

where H and H_e are the intensities of the magnetic field inside and outside the rod, respectively, l is the rod length, and N_1 is the number of turns of the solenoid surrounded by K_2 . If the solenoid is longer than the rod (this is useful for reducing the nonuniformity near the edges), then the contour can surround the solenoid winding only partially. The term

$$\frac{1}{\rho} \int_r^a E(r) dr$$

represents the field of eddy currents in the rod. The fact that these and other quantities depend on time is omitted to shorten the notation. If there is no rod in the solenoid, the integral over the outer part $BB'A'A$ of the contour K_2 , that is,

$$\frac{1}{l} \int_{BB'A'A} \mathbf{H}_e dl,$$

is usually neglected due to its smallness. We also neglect this term for the solenoid with a rod.

To obtain an approximate solution to Eqs. (A.6), (A.7), we specify a set (grid) of values of r by subdividing the cylinder cross-section into layers by concentric circles such that $r_1 = 0$ and $r_n = a$. To resolve the indeterminacy at the point $r_1 = 0$, we use the linear interpolation

$$B = B_1 + \frac{B_2 - B_1}{r_2} r, \quad r \in [r_1, r_2]. \quad (\text{A.8})$$

Then, for $E(r)$, we have the chain of equalities

$$E(r) = -\frac{1}{r} \int_0^r (\dot{B}_1 r + \frac{\dot{B}_2 - \dot{B}_1}{r_2} r^2) dr = -\dot{B}_1 \left(\frac{r}{2} - \frac{r^2}{3r_2} \right) - \dot{B}_2 \frac{r^2}{3r_2}, \quad r \in [r_1, r_2] \quad (\text{A.9})$$

and

$$E_1 = 0, \quad E_2 = -\dot{B}_1 \frac{r_2}{6} - \dot{B}_2 \frac{r_2}{3}. \quad (\text{A.10})$$

Here and in what follows, E_k, B_k, H_k ($k = 1, \dots, n$) denote the values of the corresponding quantities at the nodes. Replacing the integrals in (A.6) and (A.9) with finite sums using the trapezoidal rule, we obtain the following equations for the values at the nodes in addition to (A.10):

$$E_3 = -\frac{1}{2r_3} \left(\dot{B}_1 \frac{r_2^2}{3} + \dot{B}_2 \left(r_2 r_3 - \frac{r_2^2}{3} \right) + \dot{B}_3 r_3 (r_3 - r_2) \right), \quad (\text{A.11})$$

$$E_k = -\frac{1}{2r_k} \left(\dot{B}_1 \frac{r_2^2}{3} + \dot{B}_2 \left(r_2 r_3 - \frac{r_2^2}{3} \right) + \sum_{i=3}^{k-1} \dot{B}_i r_i (r_{i+1} - r_{i-1}) + \dot{B}_k r_k (r_k - r_{k-1}) \right), \quad k = 4, \dots, n, \quad (\text{A.12})$$

$$H_k = \frac{N_1 I_1}{l} + \frac{1}{2\rho} \left(E_k (r_{k+1} - r_k) + \sum_{i=k+1}^{n-1} E_i (r_{i+1} - r_{i-1}) + E_n (r_n - r_{n-1}) \right), \quad k = 1, \dots, n-2, \quad (\text{A.13})$$

$$H_{n-1} = \frac{N_1 I_1}{l} + \frac{1}{2\rho} (E_n + E_{n-1}) (r_n - r_{n-1}).$$

Recall that $E_1 = 0$ and $H_n = \frac{N_1 I_1}{l}$ is the intensity of the field induced by the current in the solenoid. Writing Eqs. (A.10)–(A.13) in matrix form

$$E = A_1 \dot{B}, \quad H' = A_2 E, \quad (\text{A.14})$$

and eliminating E , we obtain

$$A_{21} \dot{B} = H'. \quad (\text{A.15})$$

Here,

$$E = \begin{pmatrix} E_2 \\ E_3 \\ \vdots \\ E_n \end{pmatrix}, \quad H' = \begin{pmatrix} H_1 - \frac{N_1 I_1}{l} \\ H_2 - \frac{N_1 I_1}{l} \\ \vdots \\ H_{n-1} - \frac{N_1 I_1}{l} \end{pmatrix}, \quad \dot{B} = \begin{pmatrix} \dot{B}_1 \\ \dot{B}_2 \\ \vdots \\ \dot{B}_n \end{pmatrix}, \quad A_{21} = A_2 A_1. \quad (\text{A.16})$$

The size of the above matrices is as follows: $\dim A_1 = (n-1) \times n$, $\dim A_2 = (n-1) \times (n-1)$, and $\dim A_{21} = (n-1) \times n$. The function $B = B(H)$ and, therefore, the inverse function $H = H(B)$, is given, In the case under consideration,

$$H_k = \frac{1}{\sigma_k} a \tanh \frac{B_k}{B_s}.$$

Then, (A.15) is a system of differential equations for the unknowns B_1, B_2, \dots, B_n . It is easy to see that this system is underdetermined. It must be supplemented with the differential equation for the current I_1 in the solenoid circuit. If the solenoid is powered from an EMF source $E_0 \sin \omega t$, then this equation is

$$\mu_0 N_1^2 \pi R^2 \dot{I}_1 + I_1(R_x + R_l) = E_0 \sin \omega t + 2\pi a N_1 E_n; \quad (\text{A.17})$$

if the power supply is the current source $I_1 = I_{\max} \sin \omega t$, then the equation is

$$\dot{I}_1 = I_{\max} \omega \cos \omega t. \quad (\text{A.18})$$

For convenience, we replace the finite equation $B_n = B_s \tanh(\sigma_n H_n)$ with the differential equation

$$\dot{B}_n = \sigma_n B_s (1 - \tanh^2(\sigma_n H_n)) \frac{N_1}{l} \dot{I}_1. \quad (\text{A.19})$$

The initial conditions must satisfy the original finite equation. Systems (A.15), (A.17), (A.19) and (A.15), (A.18), (A.19) are closed systems of differential equations of order $n+1$ for the unknowns $B_1, B_2, \dots, B_n, I_1$. In the case of an EMF source, the system can be written in matrix form

$$A_3 \begin{pmatrix} \dot{B}_1 \\ \dot{B}_2 \\ \dots \\ \dot{B}_{n-1} \\ \dot{B}_n \\ \dot{I}_1 \end{pmatrix} = \begin{pmatrix} H_1 - H_n \\ H_2 - H_n \\ \dots \\ H_{n-1} - H_n \\ E_0 \sin(\omega t) - I_1(R_x + R_l) \\ 0 \end{pmatrix}.$$

Here, A_3 is a square matrix of size $\dim A_3 = (n+1) \times (n+1)$; it has the form

$$A_3 = \begin{pmatrix} a_{11} & a_{12} & \dots & a_{1n} & 0 \\ a_{21} & a_{22} & \dots & a_{2n} & 0 \\ \dots & \dots & \dots & \dots & \dots \\ a_{n1} & a_{n2} & \dots & a_{nn} & D_1 \\ 0 & 0 & \dots & 1 & D_2 \end{pmatrix},$$

where a_{ij} are the elements of A_3 , $D_1 = \mu_0 N_1^2 \pi R^2$, and $D_2 = -\sigma_n B_s (1 - \tanh^2(\sigma_n H_n)) \frac{N_1}{l}$. In the case of the current source, the system can be written in matrix form

$$A_3 \begin{pmatrix} \dot{B}_1 \\ \dot{B}_2 \\ \dots \\ \dot{B}_{n-1} \\ \dot{B}_n \\ \dot{I}_1 \end{pmatrix} = \begin{pmatrix} H_1 - H_n \\ H_2 - H_n \\ \dots \\ H_{n-1} - H_n \\ I_{\max} \omega \cos \omega t \\ 0 \end{pmatrix},$$

where

$$A_3 = \begin{pmatrix} a_{11} & a_{12} & \dots & a_{1n} & 0 \\ a_{21} & a_{22} & \dots & a_{2n} & 0 \\ \dots & \dots & \dots & \dots & \dots \\ 0 & 0 & \dots & 0 & 1 \\ 0 & 0 & \dots & 1 & D_2 \end{pmatrix}.$$

It is easy to see that the first n rows of the matrix A_3 contain the quantities that are independent of time. It is reasonable to calculate the constant part of A_3 once, and then pass it to a subroutine for calculating the right-hand sides of the differential equations via global variables because it reduces the computation time. Defining a specific function for the magnetic permeability $\mu_{\text{rod}} = \eta_{\text{rod}}(r)$ under the assumption that

$$\mu_{\text{rod}} = \left. \frac{dB}{dH} \right|_{H=0}, \text{ we obtain } \sigma = \mu_0 \mu_{\text{rod}} / B_S.$$

ACKNOWLEDGMENTS

This work was supported by the Russian Foundation for Basic Research (project no. 11-01-800e_b) and by the Ministry for Science and Education of the Russian Federation.

REFERENCES

1. B. V. Rauschenbakh, M. Y. Ovchinnikov, and S. McKenna-Lawlor, *Essential Spaceflight Dynamics and Magnetospherics* (Kluwer, Dordrecht, 2002).
2. V. I. Pen'kov and M. Yu. Ovchinnikov, "Passive Magnetic Attitude Control System for the Munin Nanosatellite," *Cosm. Res.* **40**, 142–156 (2002).
3. M. L. Battagliere, F. Santoni, M. Ovchinnikov, et al., "Hysteresis Rods in the Passive Magnetic Stabilization System for University Micro and Nanosatellites," in *Proc. 59th Cong. IAF*, Paper IAC-08.C1.8.11 (UK, Glasgow, 2008).
4. V. A. Sarychev and M. Yu. Ovchinnikov, "Satellite Magnetic Attitude Control Systems," in *Itogi Nauki Tekhn.: Ser. Issledovanie Kosmicheskogo Prostranstva* (VINITI, Moscow, 1985) [in Russian].
5. M. Long, A. Lorenz, G. Rogers, et al., "A Cubesat Derived Design for a Unique Academic Research Mission in Earthquake Signature Detection," in *Proc. of the 16th Annual/USU Conf. on Small Satellites, Logan, Utah, 2002*, paper SSC02-IX-6.
6. Y. Tsuda, N. Sako, T. Eishima, et al., "University of Tokyo's CubeSat Project—Its Educational and Technological Significance," in *Proc. of the 15th Annual AIAA/USU Conf. on Small Satellites, Logan, Utah, 2001*, paper SSC01-VIIIb-7.
7. B. Menges, A. Guadamos, K. Lewis, et al., "Dynamic Modelling of Microsatellite SPARTNIK's Attitude," in *Proc. of the 11th Annual/USU Conf. on Small Satellites, Logan, Utah, 1997*, paper SSC97-VI-2.
8. F. T. Hennepe, B. T. C. Zandbergen, and R. J. Hamann, "Simulation of the Attitude Behaviour and Available Power Profile of the Delfi-C3 Spacecraft with Application of the OpSim Platform," in *Proc. 1st CEAS European Air and Space Conf., Berlin, Germany, 2007*.
9. K. Briess, F. Baumann, and S. Trowitzsch, "Present and Future Picosatellite Missions at TU Berlin," in *Proc. of the 8th Int. Symp. of IAA on Small Satellites for Earth Observation, Berlin* (Walter De Gruyter, Berlin, 2011), pp. 49–52.
10. M. Yu. Ovchinnikov, V. D. Shargorodskii, V. I. Pen'kov, S. A. Mirer, A. D. Guerman, and R. B. Nemuchinskiy, "Nanosatellite REFLECTOR: Choice of Parameters of the Attitude Control System," *Cosm. Res.* **45**, 60–77 (2007).
11. V. A. Sarychev and M. Yu. Ovchinnikov, "Aerodynamic Attitude Control System with Hysteresis Rods," *Kosm. Issl.* **32** (6), 16–33 (1994).
12. D. S. Ivanov, S. O. Karpenko, M. Yu. Ovchinnikov, D. S. Roldugin, and S. S. Tkachev, "Testing of Attitude Control Algorithms for Microsatellite Chibis-M at Laboratory Facility," *J. Comput. Syst. Sci. Int.* **51**, 106–125 (2012).
13. D. S. Ivanov, M. Yu. Ovchinnikov, and S. S. Tkachev, "Attitude Control of a Rigid Body Suspended by String with the Use of Ventilator Engines," *J. Comput. Syst. Sci. Int.* **50**, 104–116 (2011).
14. D. Bindel', I. E. Zaramenskikh, D. S. Ivanov, M. Yu. Ovchinnikov, and N. G. Proncheva, "A Laboratory Facility for Verification of Control Algorithms for a Group of Satellites," *J. Comput. Syst. Sci. Int.* **48**, 779–787 (2009).
15. A. P. Kovalenko, *Magnetic Control Systems for Spacecraft* (Mashinostroenie, Moscow, 1975) [in Russian].
16. G. Bertotti, *Hysteresis in Magnetism* (Academic, San Diego, 1998).
17. M. L. Battagliere, F. Santoni, F. Piergentili, et al., "Passive Magnetic Attitude Stabilization System of the EduSAT Microsatellite," *Aerospace Engineering* **224**, 1097–1107 (2010).
18. M. L. Battagliere, F. Graziani, and M. Ovchinnikov, Preprint No. 65, KIAM RAS (Keldysh Institute of Applied Mathematics, Russian Academy of Sciences, Moscow, 2007). <http://library.keldysh.ru/preprint.asp?id=2007-65>.
19. R. M. Bozorth, *Ferromagnetism* (Van Nostrand, New York, 1951; Inostrannaya Literatura, Moscow, 1951).
20. V. I. Pen'kov, M. Yu. Ovchinnikov, and D. S. Ivanov, Preprint No. 31, KIAM RAS (Keldysh Institute of Applied Mathematics, Russian Academy of Sciences, Moscow, 2011). <http://library.keldysh.ru/preprint.asp?id=2011-31>.
21. W. R. Smythe, *Static and Dynamic Electricity* (McGraw-Hill, New York, 1950; Inostrannaya Literatura, Moscow, 1954).
22. A. A. Il'in, M. Yu. Ovchinnikov, and N. V. Kupriyanova, "Steady-State Rotational Motions of a Rigid Body with a Strong Magnet in an Alternating Magnetic Field in the Presence of Dissipation," *Mech. Solids* **44**, 341–351 (2009).